Mechanics of Materials 198 (2024) 105136

Contents lists available at ScienceDirect

Mechanics of Materials

journal homepage: www.elsevier.com/locate/mechmat

Research paper

AA5754 aluminium alloy springback reduction by post forming electro plastic effect (PFEPE)

Jokin Lozares [a], Nagore Otegi [b], Javier Trinidad [b], Manex Barrenetxea [c], Iosu Aizpuru [c], Pello Jimbert [d], Joseba Mendiguren [b,*]

[a] Department of Mechanics, Design and Industrial Management, University of Deusto, Avda. de las Universidades 24, Bilbao, 48007, Spain
[b] Mondragon Unibertsitatea, Faculty of Engineering, Mechanics and Industrial Production, Mondragon, Spain
[c] Mondragon Unibertsitatea, Faculty of Engineering, Electronics and Computer Science Department, Mondragon, Spain
[d] Faculty of Engineering Bilbao, University of the Basque Country, UPV/EHU, Bilbao, Spain

ARTICLE INFO

Keywords:
Metal forming
Electroplasticity
Springback
Aluminium alloy

ABSTRACT

Post Forming Electro Plastic Effect (PFEPE) has been proposed as a promising technology for mitigating forming forces and addressing springback challenges in the metal forming industry. However, several research gaps remain unaddressed for the industrialization of this technology. Firstly, there is a lack of experimental validation regarding the impact of stress reduction on springback. Secondly, the potential effect of the skin-effect on the current metrics of stress reduction needs to be evaluated. Additionally, a post-forming electrically assisted elastoplastic material model is necessary for further technology development in stamping processes. This study tackles these challenges by utilizing AA5754H22 as a reference material and integrating a comprehensive experimental campaign with finite element numerical models and empirical material model developments. Our findings confirm that PFEPE facilitates a significant reduction in springback, achieving approximately a 100% reduction. Although the skin-effect introduces non-uniform current flux density distribution, its impact at the macroscopic level is negligible for the studied thin samples. While the numerical results of springback fails to accurately replicate experimental results, the developed material model aligns well with experimental trends.

1. Introduction

In recent years, global concern over carbon footprints and CO_2 emissions has intensified. This concern is exemplified by the ambitious goal of achieving a 100% reduction in emissions for new passenger car sales starting in 2023 (Burch and Gilchrist, 2018; T.E. parliament and the Council, 2021). In response to this challenge, the automotive industry has embarked on numerous initiatives and technological advancements to meet the target of climate neutrality by 2050, primarily by reducing greenhouse gas emissions. One notable approach within this electrification-driven transformation is the pursuit of weight reduction in vehicles. It is well-documented that reducing a car's weight can contribute to lower carbon emissions, increased vehicle range, and improved battery life, as evidenced by the Carbon footprint report of the Volvo Battery electric XC40 Recharge and the XC40 ICE (Egeskog et al., 2021; Morte et al., 2023; Grosso et al., 2021).

Contrary to expectations from a decade ago (Modaresi and Müller, 2012), aluminium alloys have gained widespread acceptance as a substitute material for achieving lightweight structures. It has been estimated that a weight reduction exceeding 40% can be achieved by incorporating this material into the car's structure (Schmiedt et al., 2022; Wolfram et al., 2021; García et al., 2022). The lightweight core structure of aluminium alloys offers advantages for weight reduction strategies. However, these materials possess a lower elastic modulus compared to traditional steel, which leads to a critical springback phenomenon during forming processes (Hou et al., 2023).

The issue of springback has driven extensive research in material modelling (Mendiguren et al., 2013; Pitchure and Ricker, 2007) and the development of innovative solutions to mitigate its effects (Schuster et al., 2019; Choi et al., 2020; Hetz et al., 2020; Liu et al., 2018). Among these solutions, Electro Plastic Effect (EPE) assisted forming has gained popularity in recent years (Xu et al., 2022; Li et al., 2023; Tiwari et al., 2021). In this process, an electric current pulse train is applied to the material while it is being deformed. This superposition of the pulse train has been shown to enhance dislocation movement and reduce stresses in the material. For a more comprehensive understanding of this

* Corresponding author.
E-mail address: jmendiguren@mondragon.edu (J. Mendiguren).

https://doi.org/10.1016/j.mechmat.2024.105136
Received 22 December 2023; Received in revised form 20 August 2024; Accepted 26 August 2024
Available online 28 August 2024

phenomenon, readers are encouraged to refer to the previous work of the authors, which provides a detailed review of relevant research (Liu et al., 2022). In their previous study, the authors demonstrated the impact of EPE on pre-existing dislocation networks and its ability to rearrange these networks, thereby reducing internal stresses in the material.

In that work, the term "Post Forming Electro Plastic Effect" (PFEPE) was introduced as a distinct concept from the traditional "Electro Plastic Effect" (EPE). In EPE, an electric current pulse train is applied to the material during deformation. In contrast, PFEPE involves deforming the material without the application of an external pulse current, which is only introduced after the forming process is completed—hence the term "Post Forming." This difference in timing results in entirely different micro-mechanisms being activated. In EPE, the electric current pulse train interacts with the activation and movement of dislocations. However, in PFEPE, the pulse train interacts with an already established dislocation network. As shown in (Liu et al., 2022), PFEPE demonstrates significant potential for industrial applications, overcoming some of the limitations associated with EPE.

Additionally, Liu et al. investigated the stretch bending of Ti-50.8 at. %Ni material with superimposed electric pulse treatment and concluded that both thermal and athermal effects influence dislocation movement and vacancy behaviour during EPE. They noted that thermal effects become more prominent with increasing equivalent current density, while athermal effects are more significant with higher peak current density (Liu et al., 2021). Similar conclusions were drawn by Bao et al. in their study on Ti6Al4V pulse-assisted compression (Bao et al., 2022). Sun et al. recently examined springback reduction in AA5052 aluminium using a single pulse exceeding 70 kA and lasting less than 400 μs (Sun et al., 2022). However, in contrast to the results presented in the authors' prior study on PFEPE in AA5754H22 (Liu et al., 2022), only a modest temperature increase of 5.6 °C was observed in their study. Consequently, they suggested that athermal phenomena likely play a role in springback reduction. Xiao et al. investigated electropulsing-assisted recrystallization annealing in a cold-rolled Al-Mg-Li alloy. Their study concluded that the accelerated climb velocity of dislocations was influenced not only by the higher diffusion coefficient of vacancies generated by localized Joule heating, but also by vacancy flux resulting from electromigration. This promotion effect led to the rapid formation of substructures, which subsequently evolved into subgrains (Xiao et al., 2020). Zhao et al. determined that employing a combination of ultrasonic nanocrystal surface modification and pulse current resulted in heightened dislocation mobility, thereby inducing substantial grain refinement and a notably elevated dislocation density in the investigated 300 M steel (Zhao et al., 2020).

Numerous researchers have undertaken the challenge to disentangle the thermal and athermal effects of the Electroplastic Effect (EPE) through diverse methodologies. Hariharan et al. employed a combination of experimental and numerical analyses in their examination of tensile tests conducted on AA5052 (Hariharan et al., 2015), while Kim et al. compared EPE with direct thermal treatment on the commercial AZ31 magnesium alloy (Kim et al., 2016). At a more refined level, Kang et al. conducted an in-situ Transmission Electron Microscopy (TEM) study, concentrating on miniature test specimens to mitigate the thermal impact resulting from Joule heating (Kang et al., 2016), a technique also utilized by Li et al. with Au nanocrystals (Li et al., 2022). Taking a different approach, Andre et al. utilized an in-situ nanoindentation setup to investigate EPE in bulk eutectic Al-Al2Cu samples, whereas Gao et al. developed an electro-thermal-mechanical coupled crystal plasticity finite element model to explore the impact of nonuniformly distributed Joule heating. Recently, Liu et al. provided a comprehensive overview of contemporary electroplasticity processes, shedding light on the interplay between thermal and athermal effects (Liu et al., 2024).

However, despite the efforts of previous researchers, the origin of the Electroplastic Effect (EPE) remains unclear. Multiple underlying mechanisms occur simultaneously (Zaefferer, 2021), with no definitive ranking of which one serves as the primary driving force. Consequently, the feasibility of modelling the EPE effect remains a challenge due to the absence of a consensus on the physical phenomena involved, thereby impeding the advancement of electrically assisted manufacturing (Salandro et al., 2015).

Additionally, as early as the 1990s, Oyamada and colleagues emphasized that high current densities can disrupt the uniformity of current flow due to the skin-effect phenomenon (Oyamada et al., 1990). Under high current conditions, electric current fails to distribute evenly throughout the material (Rivas and Marti, 2002). Yuan et al. employed the frequency domain method to evaluate the depth of the current skin-effect, uncovering that the peak current density does not consistently penetrate the skin (Yuan et al., 2015). Conversely, Raicevic and Aleksic introduced a novel method for calculating pulse skin-effects in conductor materials (Raicevic et al., 2020).

Expanding on the authors' prior research, which confirmed the reduction of internal stresses in a Post Forming Electro Plastic Effect (PFEPE)-assisted stress-relaxation test for the AA575H22 material, it is crucial to highlight a significant research gap toward industrialization: the experimental validation of the impact of this stress reduction on springback has not been conducted.

Furthermore, considering the literature evidence of the skin-effect phenomenon, which may result in an uneven electrical flux, taking this phenomenon into account could substantially alter the metrics of stress reduction versus electric energy in previous study (Liu et al., 2022).

Furthermore, the absence of experimental evidence demonstrating springback reduction through Post Forming Electro Plastic Effect (PFEPE) and the lack of an elastoplastic material model for incorporation into forming simulations involving PFEPE hinder the industrialization of this technology for advancements in stamping process development.

Given the existing limitations in the current state of the art, this study is centred on advancing the understanding of Post Forming Electro Plastic Effect (PFEPE) across three distinct fronts. ① Firstly, the study empirically investigates the influence of PFEPE on v-bending springback through experimental analysis. ② Secondly, building upon these experimental findings and leveraging insights from the authors' prior work ((Liu et al., 2022)), the study evaluates the potential impact of the skin-effect on stress reduction versus electric energy metrics using numerical flux simulation models. ③ Lastly, the study develops an empirical elastoplastic material model as an initial step towards establishing a comprehensive PFEPE-elastoplastic coupled model.

2. Materials and previous results

2.1. Material description

This study centres on a 0.8 mm thick sheet of cold-rolled AA5754H22 aluminium alloy. It's noteworthy that this material aligns with the one utilized in the authors' previous investigation of PFEPE (Liu et al., 2022). Table 1 outlines the chemical composition of the examined material, while Fig. 1 illustrates the microscopic texture of the material.

Table 1
Material constants for AA5754H22 (wt.%) (Leo et al., 2016).

Si	Fe	Cu	Mn	Mg	Cr	Zn	Ti	Al
0.40	0.40	0.10	0.50	2.60–3.60	0.30	0.20	<0.15	Bal.

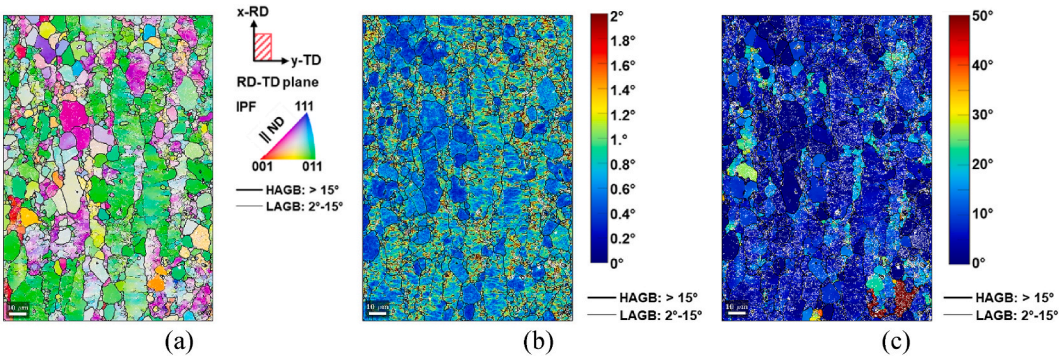

Fig. 1. Microscopic texture of the material: a) crystal orientation map, b) kernel average misorientation map and c) inner grain orientation spread map with HAGBs larger than 15° and LABGs of 2°-15° (figure modified from (Liu et al., 2022)).

2.2. Previous results

In the Discussion sections of this manuscript, frequent references will be made to the results of a previous publication authored by the researchers on PFEPE (Liu et al., 2022). To aid the reader's comprehension, the following lines provide a summary of the key findings from that study.

In their earlier study, the authors investigated the impact of PFEPE on stress-relaxation tests. During these tests, samples were elongated by 2 mm from the relaxed position, while different energy pulse trains were applied. As illustrated in Fig. 2, a reduction in force of up to 60% was observed when 6000 A·ms/mm^2 of electric charge was passed through the sample. However, it was later discussed that achieving a maximum reduction of 30% was only feasible without recrystallizing the material. It's important to note that the electric charge passing through the sample was calculated based on the sample section size of 2.5 mm × 0.8 mm (resulting in 2 mm^2).

3. Post forming electro plastic effect assisted springback experiments

This section outlines the efforts made to address the ① initial research gap concerning the absence of experimental evidence regarding springback reduction through the PFEPE technique.

3.1. Experimental procedure

Given the study's aim to evaluate springback, the v-bending test, a commonly employed experimental method (Shivaprasad et al., 2023), was chosen. An ad hoc system, as depicted in Fig. 3, was developed to serve as the pulse generator.

The ad hoc system consists of three main sub-circuits: the voltage adaptation circuit, the pre-charge circuit, and the discharge circuit. The voltage adaptation circuit utilizes an autotransformer and a three-phase diode rectifier to convert the 400 V three-phase input into a variable DC voltage, adjustable between 0 V and 540 V. The pre-charge circuit is responsible for charging the discharge circuit to the desired voltage before initiating the discharge pulse, which is managed through the control of Thyristor$_1$ (T1). The discharge circuit is specifically designed to deliver a high current pulse to the test sample by activating Thyristor$_2$ (T2). The discharge capacitor, with a total combined capacitance of 2.27 mF, and Thyristor$_2$ are crucial components, as they must handle the entire current passed through the test sample. The pulse train generated is measured using a CWT150 Rogowsky current probe from PEMUK®. A peak current of 5.87 kA was recorded at a voltage of 450 V, resulting in an energy storage per pulse of 229.83 J. The same pulse generator was utilized in the authors' previous work (Liu et al., 2022). For a more detailed description the readers are encouraged to contact the authors for further details if needed.

For this study, aluminium strips measuring 150 mm in length, 2.5 mm in width, and 0.8 mm in thickness were employed (consistent with the section dimensions used in the stress-relaxation tests conducted in the previous study).

Fig. 4, from left to right, illustrates a schematic representation of the PFEPE-assisted v-bending test procedure: Initially, the aluminium strip is positioned on the die, ensuring symmetrical distribution along the 2.5 mm × 150 mm surface. Subsequently, the v-shaped punch is lowered at an approximate velocity of 10 mm/min. The punch features a tip with a 10 mm radius and a 90° angle. To maintain consistency in the results and prevent thickness compressions at the bottom end of the v-bending punch-die, which could introduce variability, the punch stroke is limited with spacers against the die. Once the punch reaches its displacement limit, the pulse generator cables (suspended using mechanical arms to avoid the weight's impact on the sample) are connected to the sample edges, and the pulse trains are transmitted through the sample. It's worth noting that this cable connection was also employed in the reference (without pulses) testing to account for potential variations introduced by the procedure.

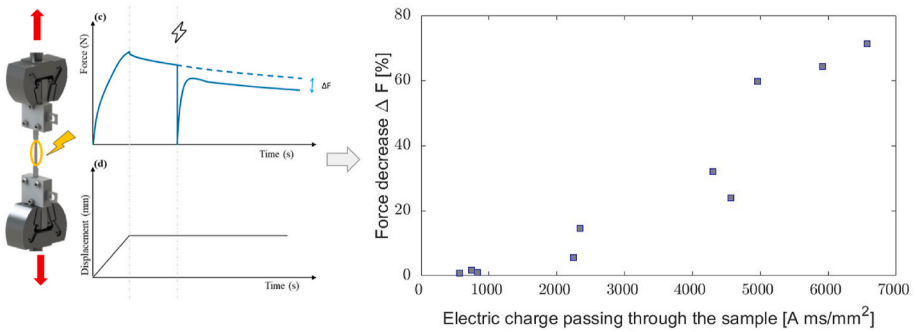

Fig. 2. Previous PFEPE work highlighted results (figure modified from (Liu et al., 2022)).

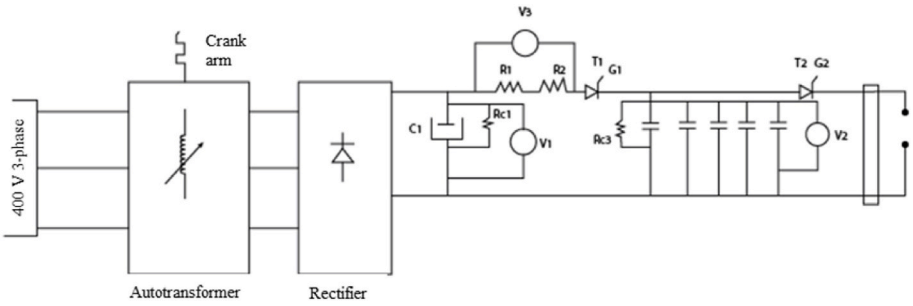

Fig. 3. Ad hoc pulse train generator architecture.

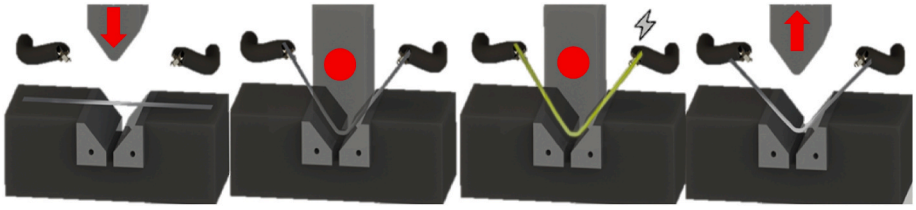

Fig. 4. Schematic representation of the PFEPE assisted v-bending springback analysis.

Following the introduction of the pulse, the sample is disconnected from the cables, and the punch is raised, releasing the sample from the die. The natural springback of the sample occurs as the punch is opened during its upward movement.

In an effort to shed light on the thermal versus athermal effect in enhancing dislocation movement (or activation in the case of Post Forming), as discussed in (Liu et al., 2024), v-bending tests were conducted under two distinct ambient conditions. Firstly, tests were performed at ambient temperature (~25 °C) with electric charge passing through the sample ranging from 500 A ms/mm^2 to 6000 A ms/mm^2. Secondly, some tests were repeated under low temperature conditions with electric charge passing through the sample ranging from 1500 A ms/mm^2 to 2300 A ms/mm^2.

Testing at cryogenic conditions using liquid nitrogen (LN_2) results in ambient temperatures of approximately −196 °C, but it comes with high resource and complexity costs. As an alternative approach, this study utilizes cryogenic testing under liquid carbon dioxide (LCO_2) due to its lower complexity. In this scenario, the ambient temperature is reduced to approximately −75 °C, (Chaabani et al., 2019).

Both room temperature (25 °C) and cryogenic temperature (−75 °C) forming steps (first two figures from the left in Fig. 4) were conducted initially at room temperature. Subsequently, for cryogenic temperature testing, a stream of liquid carbon dioxide (LCO_2) was directed towards the bending area of the sample. The electrical pulse was administered once the sample temperature reached and stabilized at −75 °C. Following this, the cryogenic stream was halted, and after the sample cooled down, the forming tools were opened to allow for springback. It's noteworthy that reference springback measurements (at 0 A ms/mm^2) were repeated under this testing protocol to ensure the consistency of the testing strategy with reference data. No differences were observed between the reference springback under cryogenic temperature and room temperature testing conditions (at 0 A ms/mm^2).

The post-forming samples underwent measurement using a goniometer, with each measurement performed a minimum of three times to ensure accuracy. In the case of the reference samples (those without electrical pulses), they exhibited a springback angle (the difference between the post-springback angle and the forming angle) of 16.44°, with a deviation of 0.27°.

3.2. Results and discussion

Fig. 5 displays the springback angle for each of the experiments. Varying electric charges passing through the sample, ranging from 0 to approximately 6000 A ms/mm^2, resulted in varying springback angles.

The springback angles (final angle minus forming angle) evolution under room temperature testing is represented by square blue markers, while the springback angles under cryogenic conditions are denoted by red triangle markers.

During the testing, a K-type thermocouple was affixed to the free bending surface of the sample to measure the temperature evolution.

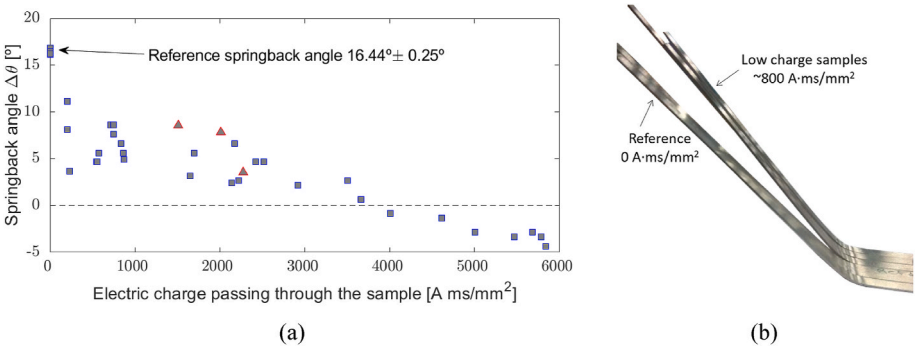

Fig. 5. PFEPE assisted v-bending springback results: a) springback angle experimental results, in blue square markers the room temperature results and in red triangles the cryogenic temperature results and b) difference between room temperature assisted and non-assisted (reference) samples represented in 0 A ms/mm^2.

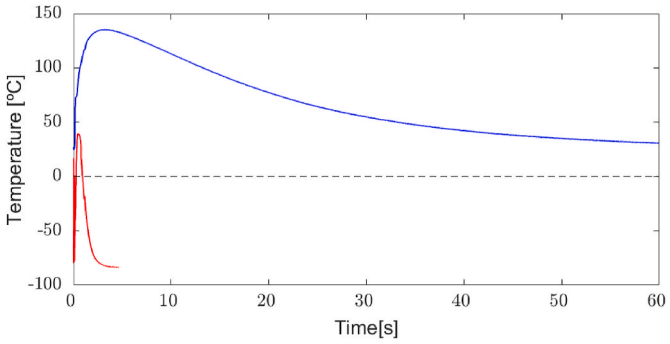

Fig. 6. Temperature evolution of the sample surface under room conditions (blue) and cryogenic conditions (red) with an electric charge of approximately 2000 A•ms/mm^2 passing through the sample.

This reading served not only to assess the stabilization of the sample under cryogenic conditions but also to record the temperature evolution during the tests under both room and cryogenic conditions.

In Fig. 6 the temperature evolution of the sample surface under room conditions is depicted in blue, while under cryogenic conditions, it is represented in red. These measurements were taken with an electric charge of approximately 2000 A•ms/mm^2 passing through the sample.

At room temperature: lower charges, specifically those below 1000 A ms/mm^2, resulted in a decrease in springback from 16.44° to approximately 5-10°. Charges in the range of ~3000–4000 A ms/mm^2 led to a decrease to ~0-3°, while charges exceeding 4000 A ms/mm^2 resulted in negative springback. Regarding the negative springback, it can potentially be associated with the recrystallization process occurring in the material under these high charge pulses, which also results in a softer post-forming material, (Liu et al., 2022). In contrast, lower to medium charge pulses were found to re-arrange dislocation structures, leading to a stress-relaxation phenomenon that could potentially reduce springback.

Under cryogenic conditions: in the range of ~1500–2500 A ms/mm^2 the room temperature tests lead to a springback angle of 4.53° ± 1.55°, considering that the reference springback angle is of 16.44°. The results of the three tests performed under cryogenic conditions lead to a springback angle of 6.66° ± 2.71°. Therefore, at room temperature the springback has been reduced in ~11.9°, this represents a reduction of ~70%, while at cryogenic conditions in ~9.8°, representing a reduction of ~60%. However, since only three samples were tested under these conditions, further studies will be necessary to provide a more robust assessment of this conclusion.

From the temperature evolution during testing depicted in Fig. 6, a distinct difference between room and cryogenic conditions in the sample temperature can be observed. It's important for the reader to note that the temperature readings were taken at the sample surface, thus extrapolations to the sample cross-section centre should be approached with caution. The figure illustrates how the Post Forming electrical pulse (approximately 2000 A•ms/mm^2) significantly increases the sample temperature in both scenarios. Under room temperature conditions, a peak temperature between 120 °C and 140 °C is reached, and it takes up to 60 s for the temperature to return to ambient conditions. In contrast, under cryogenic conditions, where the test begins at −75 °C, a peak temperature of 40 °C is reached, and the temperature stabilizes back to the ambient −75 °C in about 2.2 s.

From the current results, it is still unknown the temperature distribution at grain boundary level, (Zhang et al., 2018) under cryogenic conditions, and therefore the conclusions should be reviewed if such a data is obtained. As with many previous researchers, the authors were unable to disassociate the thermal and athermal effects. According to the authors' knowledge, reproducing such rapid temperature changes without using Joule or induction heating is not feasible, as previously stated by (Hariharan et al., 2015). Furthermore, passing a current pulse through a metallic sample without generating heat contradicts the laws of physics. Consequently, the authors compared the springback reduction generated under ambient and cryogenic conditions. These two conditions exhibit very distinct thermal paths (Fig. 6) but result in significant springback reductions (Fig. 5). Nevertheless, it is concluded that the springback reduction by PFEPE responds to something else than the global Joule effect as a reduction from ~70% of reduction to ~60% of reduction has been appreciated when reducing the temperature to cryogenic conditions.

4. Skin-effect numerical study

This second section addresses the ② second research gap, which involves evaluating the potential impact of the skin-effect on stress reduction versus electric energy metrics using numerical flux simulation models.

Examining the relationship between the force reduction observed in Fig. 2 and the impact of the same electric charge on springback experiments is essential. A summary is presented in Table 2.

The impact of high charges has already been discussed, but perhaps the most intriguing phenomenon is that low charges, which only result in <5% of force reduction in the stress-relaxation test, an *initial shock impact effect* can be appreciated in where the springback angle reduction reaches approximately 40–60%. This same trend is noticeable for the other two charge ranges as well. Both low-medium and medium-high charges were effective in significantly reducing springback while having a moderate impact on the results of the stress-relaxation test.

The authors propose a potential hypothesis related to the previously discussed skin-effect. As illustrated in Fig. 7, the bending deformation mode theoretically concentrates most of the stress on the edges of the sample (due to the linear strain gradient imposed during bending) (Marciniak and Duncan, 2002), whereas the stress-strain distribution during tension remains uniform throughout the entire cross-section.

If we consider the hypothesis that the electrical pulses employed in this study generate a skin-effect (Grimm and Mears, 2022), then the previous assumptions made in the earlier work regarding a uniform distribution of current density across the cross-section of the sample are called into question. With this in mind, it becomes apparent that the electric charge passing through the sample will result in a higher current density (and electric charge density) at the edges of the cross-section compared to the centre. Consequently, assuming that the reduction in internal stresses is proportional to the electric energy, a more significant impact will occur in a bending-type stress distribution (as the bending moment and thus springback depend on the distance from the bending centre) in contrast to the tensile test distribution.

However, it's worth noting that, at this stage, this is only a hypothesis, as the skin-effect is known to be more pronounced in thicker cross-section samples, whereas the current study utilizes a section of 0.8 mm × 2.5 mm. Therefore, the next section will focus on the numerical evaluation of the potential skin-effect under the current testing conditions.

In the following sections, two different scenarios will be considered.

- Absence of the Skin-Effect: In this scenario, it is assumed that there is no skin-effect, and the electrical flux can be considered uniform

Table 2
Summary of the impact of different electric charges in force reduction (second raw) and springback angle reduction.

	Low charges	Low-medium charges	Medium-high charges	High charges
	<1000 A ms/mm^2	2000–3000 A ms/mm^2	3000–5000 A ms/mm^2	>5000 A ms/mm^2
ΔF	<5%	5–15%	25–35%	>50%
$\Delta\theta$	~40–60%	~50–80%	%70-100	–

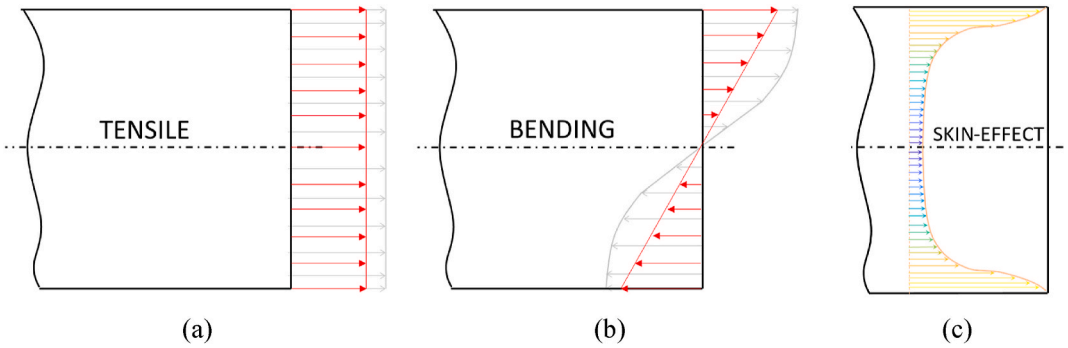

Fig. 7. Theoretical through thickness strain-stress distribution: a) tensile stress-strain distribution and b) bending stress-strain distribution, and c) skin-effect on electric current distribution through thickness. Red arrows represent the strain distribution and grey arrows the stress distribution.

across the sample section. Therefore, the following terms would be applicable:

- o *Apparent current density* J_{app} [A/mm^2]. This represents the instantaneous total current, measured at the Rogowsky current probe, divided by the cross-sectional area of 2 mm^2. It signifies the 'averaged' current density within the section.
- o *Electric charge passing through the sample* Ech_{app} [A•ms/mm^2]. This refers to the integral under the total current versus time, divided by the cross-sectional area of 2 mm^2. It represents the 'averaged' electric charge within the section.

- Presence of the Skin-Effect: In this scenario, it is assumed that the electrical flux has a non-uniform distribution across the sample section. Consequently, the following terms would be applicable:
  - o *Current density J* [A/mm^2]. This represents the instantaneous local current density. If the hypothesis of non-uniform distribution (skin-effect) is confirmed, each point within the cross-section will exhibit a distinct current density.
  - o *Electric charge density Jch* [A•ms/mm^2]. This refers to the integral under the instantaneous local current density versus time for each point within the cross-section.

4.1. Numerical procedure

Traditionally, the skin-effect has been studied as an electromagnetic phenomenon, with its characteristics strongly influenced by the pulse frequency and permeability, as governed by Maxwell's equations (Caloz et al., 2011). However, since the current study predominantly assesses single pulse scenarios, the complexity of the electromagnetic problem has necessitated the utilization of numerical tools. In this regard, QuickField® version 6.6 Element Method (FEM) software has been employed for the evaluation. The numerical study exclusively focuses on the analysis of room temperature conditions.

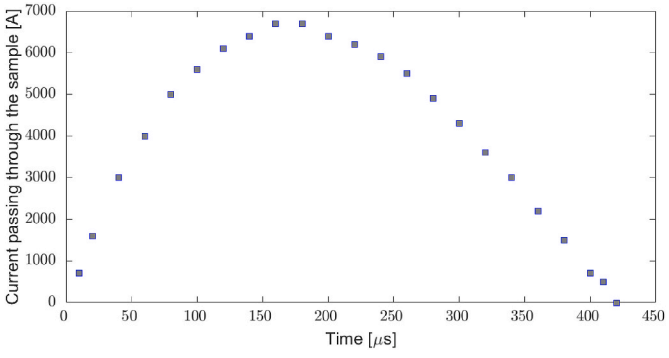

Fig. 8. Evolution of the current passing through the sample during a representative electric pulse.

Given the geometry of the samples and the transient nature of the current, a 2D Transient Magnetic problem type was chosen. The current density distribution within the sample was obtained using a time-stepping transient technique. Fig. 8 illustrates the reference electric pulse signal employed in this numerical study. The pulse accurately represents the measured pulses in both the stress-relaxation test and v-bending springback tests. The graph portrays the progression of the current passing through the sample, as measured by the Rogowsky current probe. Based on this, a solution period of 430 μs with a time step of 10 μs, chosen to ensure ample resolution, was selected. As evident in Fig. 8, the generated electrical pulse exhibits an initial increase during the first 150–170 μs, followed by a subsequent decrease up to 430 μs.

The parameters incorporated into the model for the various materials are as follows.

- For the AA5754H22 aluminium alloy:
  - o Relative Permeability: 1.00000065 (Edwards and Steer, 2016).
  - o Electrical Conductivity: 20408163 S/m (Aalco Metals Ltd, 2023).
- For the surrounding air:
  - o Relative Permeability: 1.00000037 (The Engineering ToolBox and (2016), 2023).
  - o Electrical Conductivity: 10–14 S/m (Seran et al., 2017).

4.2. Numerical skin-effect results

The numerical simulations enabled the analysis of the current density, J [A/mm^2], distribution during various stages of the electric pulse, ranging from 0 μs to 430 μs. The cross-sectional distributions at 20 μs, 120 μs, 240 μs, and 340 μs are depicted in Fig. 9. It should be noted that the significant differences in current density between the various stages have resulted in the plotting of each timestamp under different ranges.

Starting with the results at 20 μs, as shown in Fig. 9-a, this corresponds to the early stages of the electric pulse when the global current is rapidly increasing (Fig. 8). In this scenario, a clear skin-effect can be observed, where a higher density of current flows through the edges of the section rather than the centre. With an average current density around J = 800–900 A/mm^2, a noticeable global difference of about 80 A/mm^2 (~9%) can be observed between the extreme values.

At a later stage of the pulse, around 120 μs, when the current is beginning to lose its rapid increase, as depicted in Fig. 9-b, the skin-effect is still present, but the differences are significantly reduced. With an average current density around J = 3040–3080 A/mm^2, a global difference of about 30 A/mm^2 (~1%) can be noticed. This is due to the fact that the current increment is less aggressive, favouring a more uniform distribution.

When examining the results during the downward phase of the pulse, with the distribution at 240 μs in Fig. 9-c, and 340 μs in Fig. 9-d, the opposite current density distribution is observed. In this case the current derivative *di/dt* has the opposite direction, thus the direction of the

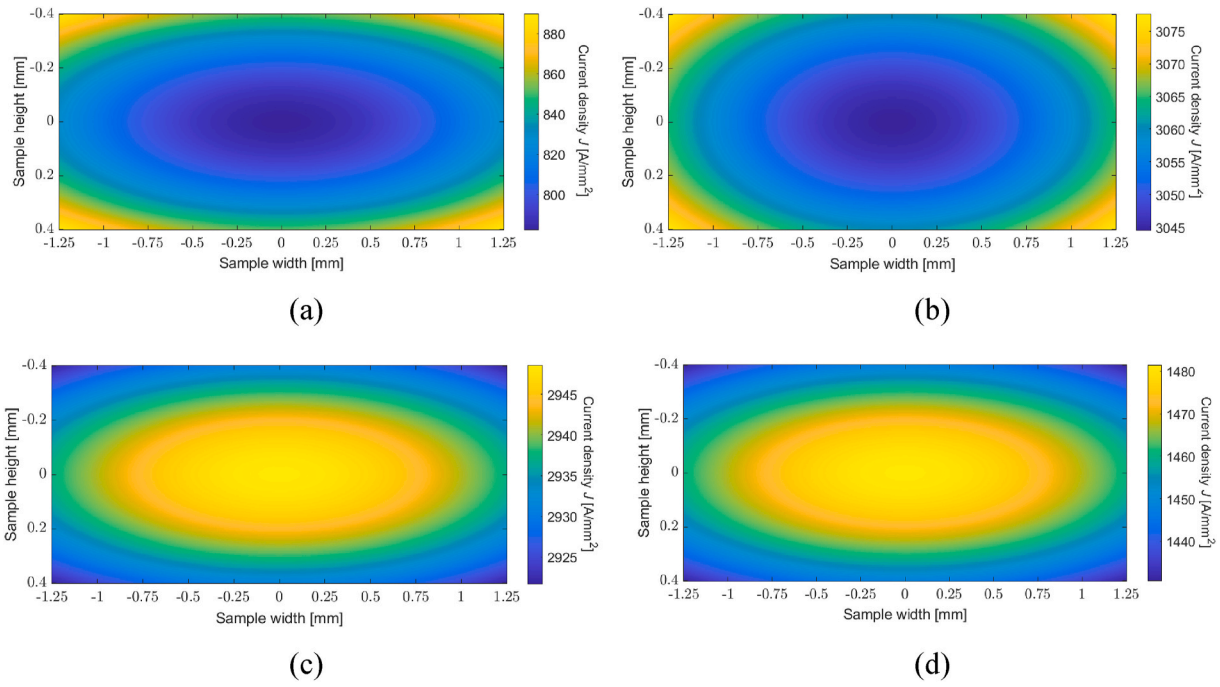

Fig. 9. Current density over the 2.5 mm × 0.8 mm cross-section area under a) 20 μs, b) 120 μs, c) 240 μs, and d) 340 μs. It should be noted that the significant differences in current density between the various stages have resulted in the plotting of each timestamp under different ranges.

induced Eddy currents is also flipped. Unlike previous scenarios where the current density in the edges is increased for a rapidly increasing current, a rapidly decreasing current will have the opposite effect, decreasing the current density in the edge, and obtaining a highly centred-concentrated current density (Yan and Chen, 2023).

To quantify the heterogeneity of the current density distribution generated by the skin-effect, three distinct edge values have been compared with the central value. Along the X-axis, the value at the edge of the horizontal axis, with coordinates [1.25, 0] in Fig. 9, has been compared to the centre of the sample, denoted as [0, 0]. On the Y-axis, the value at the edge of the vertical axis, [0.4, 0], has been used as a reference, and for the D (diagonal) axis, the value at the corner of the sample, [1.25, 0.4], has been employed. Fig. 10 illustrates the percentage difference between the reference values and the centre of the specimen at various time intervals during the pulse.

The first notable conclusion is the dependence of the direction of the difference on the increasing and decreasing phases. Additionally, it's important to note that the largest differences occur at both extremes of the pulse signal, where the increase or decrease appears to be steeper

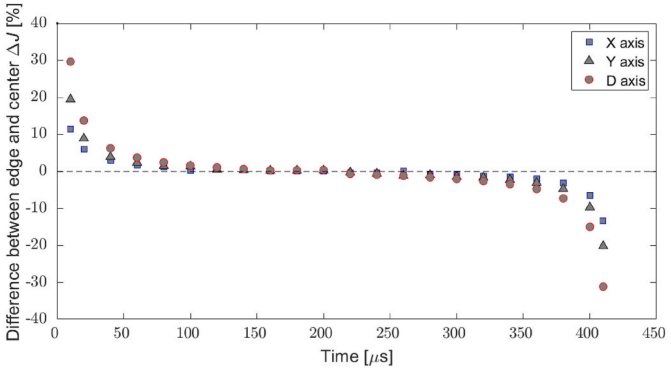

Fig. 10. Differences at current density, J, between the edge and the centre. In square markers the difference taking the edge at the x axis. In triangle makers taking the edge of y axis and in rounds taking the diagonal.

compared to the central part of the pulse. In these extreme cases (at the beginning and end of the pulse), differences of about 10–30% can be observed, while during most of the pulse duration, between 60 μs and 340 μs, a more homogeneous distribution is evident.

Furthermore, it's worth considering that the central segments of the pulse (approximately 80 μs–300 μs) exhibit higher current density passing through the sample. To illustrate, consider the comparison between the distributions at 20 μs and 120 μs, where the averaged current density increases from J ~850 A/mm^2 to J ~3050 A/mm^2.

From these results, it is evident that the current pulses employed in this study generate a skin-effect during certain parts of the pulse, as seen in Fig. 9. This implies that the electric charge density, measured in A•ms/mm^2, will vary depending on whether a material point is at the edge of the sample or in the centre of the cross-section. However, the distribution of the current density is directly related to the tendency of the pulse. During the upgoing phase (between 0 μs and 170 μs), the skin-effect leads to an increase in current density at the edges of the cross-section, while during the downgoing phase (between 170 μs and 430 μs), the distribution reverses, with higher values in the centre of the cross-section. Moreover, the most heterogeneous distributions occur during time steps when there is a moderate to low average current density passing through the sample, whereas during peak average density time steps, the distribution becomes more homogeneous.

To visualize the potential skin-effect on Electric Charge Density, the relative density across the section is presented in Fig. 11. The relative density, denoted as $\rho_{(i,j)}$, is calculated as follows:

$$J\mathrm{ch}_{(i,j)} = \rho_{(i,j)} \bullet E\mathrm{ch}_{\mathrm{app}}, \tag{1}$$

where $J\mathrm{ch}_{(i,j)}$ represents the electric charge density at each coordinate.

It must be noted that even if the whole range of colours (blue to yellow) is used, the variations only differ between 0.99665 and 0.99685 in both extremes. On one hand, a distinct skin-effect can be observed, where a higher density extends beyond the section's boundaries. On the other hand, the discrepancies between the extremes are on the order of 0.0002. Consequently, assessing whether these differences are significant enough to induce the effect illustrated in Fig. 7 is challenging.

At this stage of the study, it can be concluded that the specific

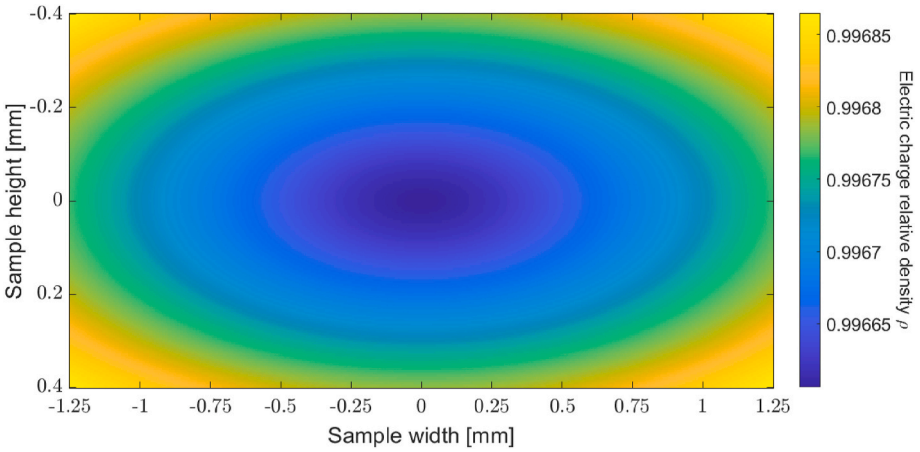

Fig. 11. Electric charge relative density ρ over the section of the sample.

scenario under investigation, which includes a reduced sample cross-section, pulse characteristics, and current amplitude, leads to an insignificant heterogeneity in current density and electric charge density relative to the skin-effect. In the following section, an empirical PFEPE-assisted elastoplastic model will be developed, and it will be used to initially evaluate whether the slight differences could be responsible for the experimentally observed differences and the identified *initial shock impact effect*.

5. Modelling of the PFEPE assisted stress-relaxation and v-bending springback test

This third section addresses the ③ third research gap of development of an empirical elastoplastic material model as an initial step towards establishing a comprehensive PFEPE-elastoplastic coupled model.

The developed material model adopts an empirical approach based on observed elastoplastic data. This initial approach will be calibrated using the stress-relaxation data observed in Fig. 7 under different scenarios, considering or not considering the skin-effect, and assuming different relationships between the stress relaxation and the electric current flux metric. The objective of the developed material model is twofold. First, the material model, in conjunction with a mechanical representation of the forming and springback processes, will serve as a tool to evaluate the potential impact of the predicted minimal skin effect in elucidating the *initial shock impact phenomenon*. Secondly, the material model aims to serve as an initial preliminary model for further research to construct PFEPE models that will facilitate the upscaling of the technology.

5.1. Fundamental material model

The underlying principle of the classic elastoplastic theory lays in the assumption of addition of the elastic, $\boldsymbol{\varepsilon}^{e}$, and plastic strain, $\boldsymbol{\varepsilon}^{p}$. The corresponding rate for of the additive reads:

$$\dot{\boldsymbol{\varepsilon}} = \dot{\boldsymbol{\varepsilon}}^{e} + \dot{\boldsymbol{\varepsilon}}^{p}, \tag{2}$$

where $\boldsymbol{\varepsilon}$ represents the total true strain. On top of that, Hooke's law stablishes the relation between the elastic strains (associated with the crystallographic plane distance) and the stress tensor rate, $\dot{\boldsymbol{\sigma}}$,

$$\dot{\boldsymbol{\sigma}} = \mathbf{D}^{e} : \dot{\boldsymbol{\varepsilon}}^{e}, \tag{3}$$

where $\mathbf{D}^{e}$ represents the standard isotropic elasticity tensor (de Souza et al., 2008). The plastic flow may occur when the stress state reaches a certain level (Banabic et al.), satisfying the following relation,

$$\Phi(\boldsymbol{\sigma}, \boldsymbol{A}) = 0, \tag{4}$$

in where the scalar yield function, Φ, is function of the stress tensor and a set of hardening thermodynamical forces, $\boldsymbol{A}$. In the particular case of the elastic domain, the stress forces do not reach the hardening forces values, and the nature of the yield function assures that $\Phi < 0$ for those cases. Once the plastic flow occurs, the material will plastically deform, proportional to the plastic flow vector, $\boldsymbol{N}$, and the scalar plastic multiplier, $\dot{\gamma}$,

$$\dot{\boldsymbol{\varepsilon}}^{p} = \dot{\gamma} \bullet \boldsymbol{N}. \tag{5}$$

The plastic flow it is assumed to follow the normality rule (de Souza et al., 2008, Banabic et al),

$$\boldsymbol{N} = \frac{\partial \Psi}{\partial \boldsymbol{\sigma}}, \tag{6}$$

where Ψ, represents the plastic potential. For the sake of simplicity, in this study the associated flow rule theory will be followed assuming $\Psi = \Phi$ (Mendiguren et al., 2018). The hardening forces, $\boldsymbol{A}$ account for the hardening variables, $\boldsymbol{\alpha}$,

$$\dot{\boldsymbol{\alpha}} = \dot{\gamma} \bullet \boldsymbol{H}, \tag{7}$$

where $\boldsymbol{H}$ corresponds to the generalised hardening modulus which defines the evolution of the hardening variables, and it is derived from the same potential,

$$\boldsymbol{H} = -\frac{\partial \Psi}{\partial \boldsymbol{A}}. \tag{8}$$

Under elastic state, no hardening will be developed and therefore $\dot{\gamma} = 0$. While during plastic deformation $\dot{\gamma} > 0$. That leads to the consistency condition of $\Phi \bullet \dot{\gamma} = 0$.

A Swift-Hockett/Sherby hardening model (Agirre et al., 2018) has been used in this work for the evolution of the yield stress, σ_y, with the following expression

$$\sigma_y = C_1 \bullet (\varepsilon_0 + \overline{\varepsilon}^{p})^{C_2} + C_3 \bullet \exp\left(-C_4 \bullet (\overline{\varepsilon}^{p})^{C_5}\right), \tag{9}$$

where $\overline{\varepsilon}^{p}$ stands for the internal scalar variable, accumulated plastic strain (de Souza et al., 2008). In this work, the von Mises effective plastic strain will be assumed leading to

$$\overline{\varepsilon}^{p} = \int_{o}^{t} \sqrt{\frac{2}{3}\dot{\boldsymbol{\varepsilon}}^{p} : \dot{\boldsymbol{\varepsilon}}^{p}}\, dt \longrightarrow \dot{\overline{\varepsilon}}^{p} = \dot{\gamma}, \tag{10}$$

leading to

$$\Phi\left(\sigma_{eq} - \sigma_{y}\right) \leq 0, \tag{11}$$

where σ_{eq} represents the scalar equivalent stress.

As previously mentioned, in this work, for the sake of simplicity and under the assumption that the anisotropy of the AA5754H22 will not play an important role on the stress-relaxation and v-bending modelling, a von Mises equivalent stress will be assumed (Banabic et al.), following the expression

$$\sigma_{eq} = \sqrt{3 \bullet J_2(\boldsymbol{s}(\boldsymbol{\sigma}))}, \tag{12}$$

where $J_2(\boldsymbol{s}(\boldsymbol{\sigma}))$ represents the second invariant of the deviatoric component of the stress tensor.

5.2. PFEPE incorporation in the material model

Based on our previous findings and the work conducted in (Liu et al., 2022), we can make the assumption that PFEPE reorganizes the dislocation network of the material, thereby reducing internal stresses. Following a mechanism similar to that in a stress-relief annealing process, various micro mechanisms are activated at the atomic level by the energy supplied to the system. Fig. 12 illustrates several of these mechanisms. Fig. 12-a depicts the development of dislocation tangles during deformation. As the system's vibration ability increases (whether due to the effects of Joule heating or other athermal effects such as electron winds (Liu et al., 2024)), the dislocation network tends to reorganize and annihilate towards cell formation, as shown in Fig. 12-b and c. Fig. 12-d schematically represents a scenario in which two adjacent but mirrored dislocations annihilate each other, either by gliding in the same plane (A and B) or by a combination of glide and climb (C and D), (Humphreys and Hatherly, 2004). Finally, Fig. 12-e to g depict a schematic scenario of elastic strain conversion to plastic strain. Fig. 12-e illustrates an atomic distribution surrounding a dislocation. When a force is applied to the system and deformation is forced but not enough to trigger dislocation movement, the structure adapts by elastic strain and therefore internal stresses (Fig. 12-f). However, if the system is excited (by thermal or athermal processes), the ability of the atoms to move/vibrate will increase, and they will rearrange towards a lower energy position, converting the elastic strain into permanent lower energy plastic strain.

The hypothesis that during an annealing process, where stress relief occurs, elastic strains convert to plastic strain was introduced by Vierck et al., in 1991 (Viereck et al., 1991). According to Hooke's law, stresses are directly related to the interatomic plan out-of-equilibrium elastic strain (de Souza et al., 2008). Therefore, elastic strains and internal stresses are proportional to each other. The only way to reduce these internal stresses is by reducing the elastic strains, and according to classical elastoplastic theory, if the total strain is not modified, the only option is for the atomic distribution to be rearranged and the elastic strains to be absorbed by plastic strain.

Consequently, during PFEPE, some of the elastic strains are absorbed by the emergence of new plastic strains through the reorganization of internal dislocation structures and generation of dislocation substructures. For a visual representation of this process, please refer to Fig. 13.

Fig. 13-a shows the original stress-strain path during a uniaxial tensile and relaxation. The material begins at the origin in a relaxed state (point A). Upon stretching the material, it reaches point B, where a specific stress-strain state $(\varepsilon_B, \sigma_B)$[†] is attained. At the uniaxial level, the stress state is governed by Hooke's law $\left(\sigma_B = E \bullet \varepsilon_B^e\right)$, in where E represents the Young modulus (Marciniak and Duncan, 2002). Additionally, the strain level is divided into elastic and plastic component $\left(\varepsilon = \varepsilon_B^p + \varepsilon_B^e = \varepsilon_B^p + \sigma_B / E\right)$. Subsequently, when the sample is unloaded until point PS_1, some of the elastic strain is recovered, thereby reducing the associated stresses.

Fig. 13b depicts the PFEPE-assisted uniaxial tensile and relaxation. In this scenario, between point B and point C, there is a transfer of strains, resulting in a reduction of elastic strains while increasing plastic strains to compensate, thereby maintaining constant total strains. As a result, the elastic recovery will be smaller.

$$\varepsilon_C = \varepsilon_B \;\&\; \sigma_C < \sigma_B \longrightarrow \varepsilon_C^e < \varepsilon_B^e \longrightarrow \varepsilon_C^p > \varepsilon_B^p \longrightarrow \left(\varepsilon_C^e + \varepsilon_C^p = \varepsilon_B^e + \varepsilon_B^p\right). \tag{13}$$

In the stress-relaxation scenario, we consider two theories for the relationship between electrical pulses and stress relaxation.

- T1. The electric charge passing through the sample 'Ech_{app} [A•ms/mm^2]'.
- T2. The electric charge density 'Jch [A•ms/mm^2]'.

It should be noted that T1 theory neglects the potential impact of the skin-effect, while T2 assumes a heterogeneous distribution of the current density.

5.3. Mechanical representation of the forming and springback processes

For the mechanical representation of the forming and springback process, the cross-section presented in Fig. 9 will be utilized. Symmetry will be assumed, and only the first quadrant will be studied (X from 0 to 1.25, and Y from 0 to 0.4). The section of interest will be divided into N_X x M_Y cells. Therefore, the size of each cell will be ($1.25/N_X$ x $0.4/M_Y$). After a convergence study, $N_X = 300$ and $M_Y = 100$ have been determined as the optimal and efficient discretization steps. For the calculation of the force in the stress-relaxation scenario, the following expression will be used:

$$F = \int_{x=-1.25}^{x=1.25} \int_{y=-0.4}^{y=0.4} \sigma_z \, dydx = \int_0^A \sigma_z \, dA, \tag{14}$$

where, σ_z corresponds to the stress in the Z direction (perpendicular to the section) and A corresponds to the whole cross-sectional area. If the expression is numerically evaluated, then,

$$F \cong 4 \bullet \sum_{i=1}^{N_X} \sum_{j=1}^{M_Y} \sigma_z(i,j) \bullet A_c, \tag{15}$$

where A_c represents the area of the cell. For the v-bending springback test, the bending neutral axis is assumed in the coordinate system and therefore, the bending moment M can be defined as

$$M = \int_{x=-1.25}^{x=1.25} \int_{y=-0.4}^{y=0.4} \sigma_z \bullet y \, dydx \cong 4 \bullet \sum_{i=1}^{N_X} \sum_{j=1}^{M_Y} \sigma_z(i,j) \bullet y_{ij} \bullet A_c, \tag{16}$$

where y_{ij} represent the distance in Y axes from the coordinate centre to the centroid of the cell. The location of the bending neutral axis follows the classic bending theory considering that the thickness of the samples is of 0.8 mm compared to the 10 mm radius of the punch tip (Marciniak and Duncan, 2002).

5.4. Calibration of the material model

The developed mechanical representation of the forming and springback process relies on the imposition of a strain field evolution in the cross-section of the sample. These modelling techniques are widely used in the industry for optimization purposes (Silvestre et al., 2016). However, the current experimental validation study's boundary conditions (BC) are geometric features of the punch and die. Therefore, to establish the correct strain field evolution occurring in the cross-section during the v-bending test, a finite element model was employed.

The total strain resulting from the uniaxial tensile stretching of the stress-relaxation tests follows a simple relation to the stretching and the calibrated length (Liu et al., 2022). However, to ensure consistency and avoid miscalculations stemming from the approximation of the

[†] For the sake of simplicity uniaxial terms will be used in this explanation.

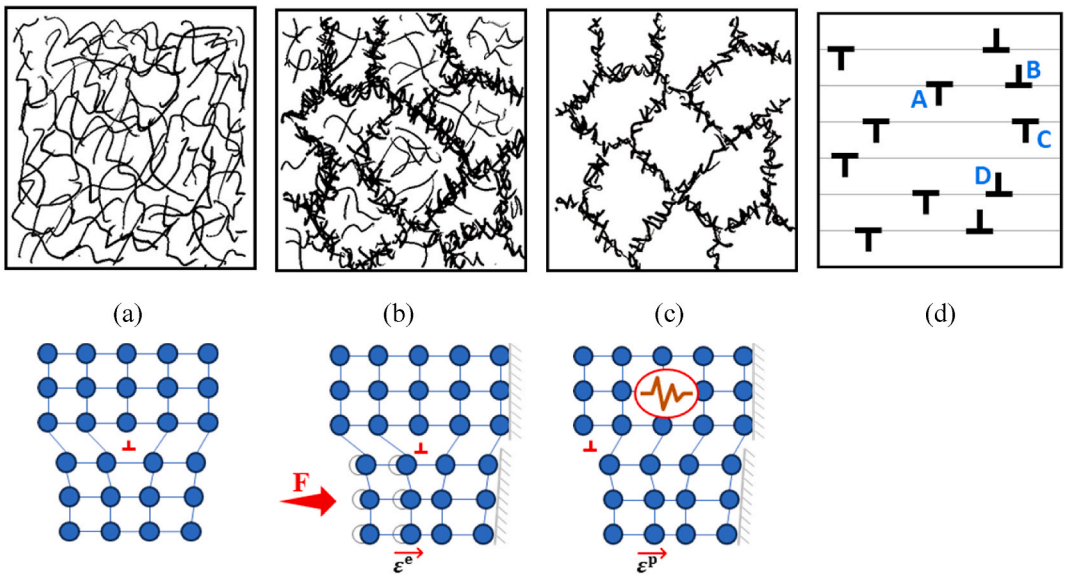

Fig. 12. Internal stress reduction by dislocation rearrangement (figure modified from (Humphreys and Hatherly, 2004)). a) to c) dislocation tangles to cell formation by dislocation rearrangement and annihilation. d) Dislocation annihilation by glide and climb mechanisms. e) to g) elastic strain conversion to plastic strain by atomic vibration.

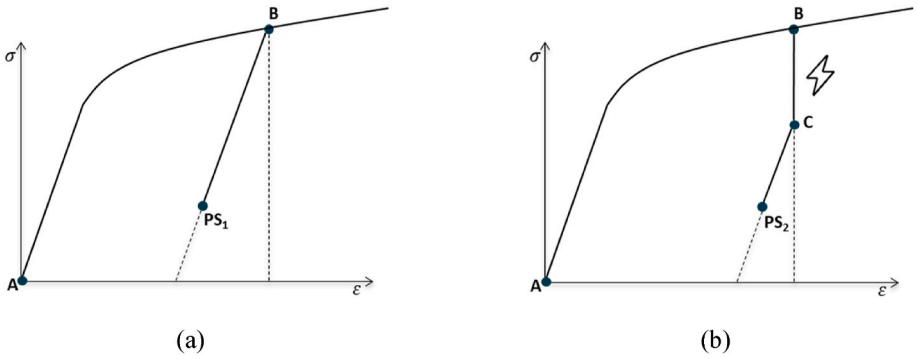

Fig. 13. Schematic representation of the PFEPE phenomenon at uniaxial tensile level: a) original state of deformation and unloading, and b) PFEPE assisted unloading.

calibrated length of the sample, the system was modelled in Abaqus/-Standard®. The simulation utilized a total time step of 1 s, with an initial and maximum increment size of 0.01 s, and a minimum of $1 \bullet 10^{-5}$. The cross-section was divided into 3D linear brick reduced integration elements (C3D8R) with dimensions $\Delta x = \Delta y = \Delta z = 0.08$ mm. The simulation revealed that a total strain of $\varepsilon_Z = 5.66\%$ was achieved after the initial 2 mm of pre-stretching.

By utilizing the relation between displacement and strain obtained from the simulation and comparing it with the tensile experimental results from previous work (Liu et al., 2022), the parameters of the Swift-Hockett/Sherby hardening model were determined through a best-fitting strategy. These parameter values are presented in Table 3.

5.5. Calibration of the different theories

Following the calibration of the base material behaviour, this section focuses on calibrating the various theories that establish the relationship between electrical pulses and stress relaxation.

Table 3
AA5754H22 material Swift-Hockett/Sherby hardening model parameters.

C_1	C_2	C_3	C_4	C_5	ε_0
410.000 MPa	0.237	0.815 MPa	0.311	10.470	0.023

5.5.1. T1. The electric charge passing through the sample 'Ech_{app} [A•ms/mm^2]'

To calibrate the reduction of stress based on the electric charge passing through the sample, we first use the data presented in Fig. 2, which shows the decrease in force. Then, we apply the relationship shown in Eq. (14) and assume a constant distribution to obtain the evolution of the stress decrease, denoted as σ_z, which is calculated as $\sigma_z = F/(2\,\mathrm{mm}^2)$. Since the data in Fig. 2 is in percentage, and the relation is proportional, the percentage values remain the same for $\Delta\sigma_z$. Finally, we fit a second-order polynomial relation to the data using the least squares method. The obtained relation, with an R-squared value of 0.93, is as follows:

$$\Delta\sigma_z = 1.5860 \bullet 10^{-6} \bullet \left(E\mathrm{ch}_{\mathrm{app}}\right)^2 + 0.0011 \bullet \left(E\mathrm{ch}_{\mathrm{app}}\right) - 0.7319, \quad (17)$$

where $E\mathrm{ch}_{\mathrm{app}}$ is measured in (A•ms/mm^2) while $\Delta\sigma_z$ is in percentage.

5.5.2. T2. The electric charge density 'Jch [A•ms/mm^2]'

The calibration of the second theory is not as straightforward as T1. First, it has to be considered that the reduction of the force can be represented as the difference between force at stage 0 (prior-pulse) and force at stage 1 (post-pulse),

$$\Delta F\,[\%] = (F_0 - F_1)\,/\,F_0, \quad (18)$$

$$\Delta F\ [\%] = \left(\sum \sigma_z(i,j)_0 - \sum \sigma_z(i,j)_1\right) \Big/ \left(\sum \sigma_z(i,j)_0\right), \tag{19}$$

and as the initial stress is constant though the section, this leads to

$$\Delta F\ [\%] = \frac{\sum \Delta\sigma_z(i,j)}{(N_X \bullet M_Y)}, \tag{20}$$

where $\Delta\sigma_z(i,j)$ represents the reduction in stresses in percentage for each cell.

Next, for the sake of simplicity, we assume that, in this case as well, the relation between electric charge density and stress reduction follows a second-order polynomial. Therefore, the only unknowns are the parameters of the polynomial model that fit the reduction of stresses for all experiments. To obtain these parameters, we use an unconstrained multivariable function and the derivative-free method 'fminsearch' in Matlab®.

Under this second hypothesis, the relation between the electric charge density and the stress reduction can be found as,

$$\Delta\sigma_z = 1.4601 \bullet 10^{-6} \bullet (J\mathrm{ch})^2 + 0.0014 \bullet (J\mathrm{ch}) - 0.6743 \tag{21}$$

When assessing the precision of both theories in depicting force reduction, Fig. 14 illustrates the predictions of both. Both theories exhibit a satisfactory alignment with the experimental data. Furthermore, the minimal variance in the coefficients implies that, at the stress-relaxation level, the impact of the skin-effect on the outcomes was negligible.

5.6. Validation of the PFEPE theories

To validate against the v-bending springback experiments the mechanical representation of the forming and springback process utilizes bending theories developed by Marciniak et al. in the early nineties (Marciniak and Duncan, 2002). This theory combines a plane strain assumption along the bending line with a plane stress assumption through the thickness. When combined with von Mises theory, it simplifies Eq. (12) to $\sigma_{eq} = \sqrt{3}/2 \bullet \sigma_z$, and Eq. (10) to $\dot{\bar{\varepsilon}}^p = 2/\sqrt{3} \bullet \dot{\varepsilon}_z^p$. Additionally, the elastic relation in Eq. (3) can be rewritten as $\sigma_z = E/(1-\nu^2) \bullet \varepsilon_z^e$, where ν represents Poisson's ratio (assumed to be 0.3) and E represents the elastic modulus (taken as 70 GPa).

Following the same approach as in the stress-relaxation section, a numerical simulation has been conducted under plane strain conditions with square linear plane strain reduced integration elements (CPS4R) having $\Delta y = \Delta z = 0.08$ mm. This numerical simulation is used to convert displacement boundary conditions to strain states and vice versa. Explicit resolution has been selected with a tangential frictionless penalty contact algorithm.

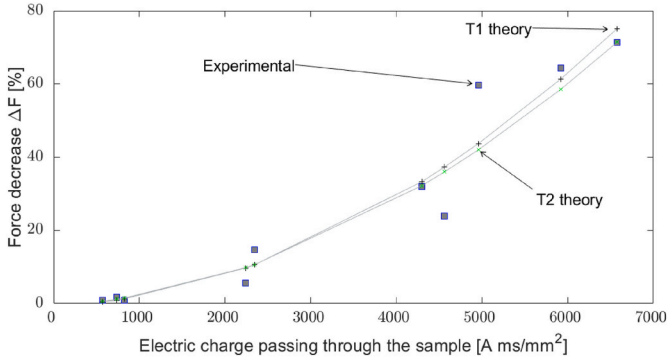

Fig. 14. Comparison of the experimental force decrease with the predictions of both T1 and T2 theories. Experimental data is represented by blue markers, while the continuous line and '+' and 'x' markers indicate the predicted values by both models.

The mechanical representation of the forming and springback process has been developed as follows.

1. Beginning with the imposed forming strain distribution, the stress and elastoplastic state (plastic and accumulated plastic strain) have been calculated at each cell in the quarter-section under analysis.
2. An elastic predictor-plastic corrector algorithm has been implemented using a MATLAB® code (Mendiguren et al., 2013), adhering to the assumption established by Marciniak et al. that the plane normal section will remain plane during bending (Marciniak and Duncan, 2002).
3. Upon completion of the forming process, the stress reduction, contingent upon the electric charge passing through the sample (Ech_{app}), and the theory (T1 or T2), has been applied.
4. Subsequently, the springback calculation is performed from the post-pulse state. Springback is computed as the equilibrium state where the bending state results in a zero-value moment, Eq. (16). This state is obtained through an iterative process involving an unconstrained multivariable function using the derivative-free method 'fminsearch' in MATLAB®, combined with moment calculation and the elastic predictor-plastic corrector algorithm.

Fig. 15 depicts representative forming and springback profiles through the thickness, which are outcomes of the described mechanical representation of the forming and springback process.

In the strain distribution figure, the elastic recovery is illustrated, while in the stress distribution figure, the compensation of the moment generated by the stresses can be observed.

Utilizing this methodology, the reduction in springback angle dependent on the electric charge passing through the sample, following both T1 and T2 theories, has been calculated. The predictions of each theory, along with the room temperature experimental results, are presented in Fig. 16.

At first glance, a notable disparity between the mechanical representation of the forming and springback process predictions and the experimental results is evident. While the mechanical representation of the forming and springback process predictions capture the general trend of the experimental results, they deviate by approximately 40%. This deviation corresponds to the *initial shock impact effect* in springback angle observed in the experimental results at low charges (Table 2). Upon closer scrutiny, there doesn't appear to be a significant discrepancy between the predictions of the T1 theory and the T2 theory. Surprisingly, the T2 theory, which considers the skin-effect and was anticipated to result in a higher reduction in springback angle (Fig. 7), actually predicts a slightly lower value compared to the T1 theory. This could be elucidated by the marginal difference in fitting shown in Fig. 14, suggesting that the skin-effect observed in this study may not exert a substantial impact on the overall stress relaxation behaviour.

6. Discussion

This study is centred on advancing the understanding of Post Forming Electro Plastic Effect (PFEPE) across three distinct fronts. ① Firstly, the empirical investigation of the influence of PFEPE on v-bending springback. ② Secondly, the evaluation of the potential impact of the skin-effect on stress reduction versus electric energy metrics using numerical flux simulation models. ③ Lastly, the development of an empirical elastoplastic material model as an initial step towards establishing a comprehensive PFEPE-elastoplastic coupled model.

① Post Forming Electro Plastic Effect (PFEPE) Springback experiments

The primary finding from the experiments is that PFEPE serves as an effective method for reducing springback in the analysed alloy and conditions. Employing pulses within the safe range, as identified in the

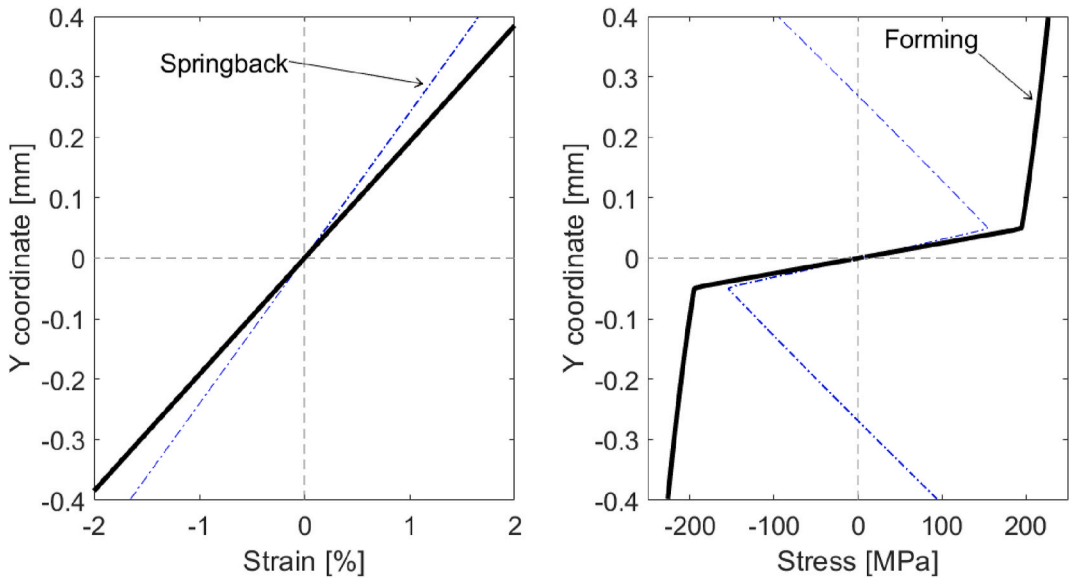

Fig. 15. Representative forming (in thick black line) and springback (in dash-doted blue line) profiles of strain and stress distribution through thickness.

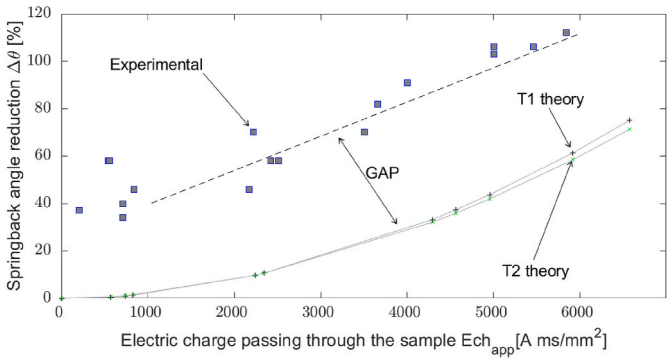

Fig. 16. Springback angle reduction experimental and mechanical representation of the forming and springback process predictions with both T1 and T2 theories. Blue markers represent the experimental data (under room conditions) while the continuous line and '+' and 'x' markers indicate the predicted values by both models. A clear gap can be appreciated between both tendencies.

previous publication (Liu et al., 2022), leads to a reduction in the springback angle ranging from 40% to nearly 100%.

Another significant observation is that, in contrast to stress-relaxation data, low charge pulses develop an *initial shock impact effect* that results in a 40%–60% reduction in springback. These results raise new questions due to the substantial impact on springback despite the moderate effect on stress-relaxation (Table 2). Nevertheless, the validation of the PFEPE technique suggests the potential to reduce not only springback but also structural residual stresses.

The origin of the observed reduction remains unclear. Analysis of the test conditions reveals a variation in angle reduction from approximately 70% at room temperature to about 60% under cryogenic conditions. The scientific community is divided between those who attribute the impact of electric pulses on dislocation behaviour to thermal effects and those who argue for the significance of athermal effects. The current results suggest a combination of both thermal and athermal effects.

During cryogenic testing, the thermal energy introduced to the sample was significantly reduced compared to room temperature testing, as indicated by the temperature evolution at the sample surface previously reported. This reduction in temperature led to a decrease in springback reduction from 70% to 60%, underscoring the role of thermal effects. Nevertheless, despite the minimal thermal energy introduced in the cryogenic tests, the springback angle reduction still reached 60%. This suggests that either the small amount of thermal energy is sufficient to relax dislocations or that athermal effects play a significant role in dislocation relaxation.

However, given that only three samples were tested under these conditions, additional studies are required to provide a more robust evaluation of these conclusions. It is also important to note that these results are specific to the AA5754H22 material with a thickness of 0.8 mm and a cross-sectional area of 2 mm^2, using the pulse characteristics described in previous sections. Different test conditions or material configurations could yield varying results.

② Skin-effect numerical simulations

The study demonstrates that the characteristics of the electrical pulse used in this investigation, as shown in Fig. 8, in combination with the studied sample geometry, generate a skin-effect in the distribution of current flow across the sample cross-section, as depicted in Fig. 9. However, the heterogeneity produced by this effect is concentrated at the beginning and end of the pulse, where a sharp change in current is observed. These differences decrease as the pulse amplitude increases and become negligible at the peak of the pulse (Fig. 10). Consequently, while some current density heterogeneity is evident (Fig. 11), it appears unlikely to have a significant impact on the results at the current study's scenario.

The assessment of the skin-effect's influence on PFEPE-induced springback reduction, as proposed in Fig. 13, highlights that the generated heterogeneity at the current density level (Fig. 11) is insufficient to significantly affect the angle reduction. Consequently, the hypothesis does not receive validation.

③ PFEPE assisted material model and the mechanical representation of the forming and springback process

A comprehensive PFEPE assisted material model has been formulated. In this study, the overall model has been adapted to two distinct theories: T1, where stress reduction depends on the electric charge passing through the sample, and T2, where stress reduction depends on electric charge density. Regardless of the validation outcome for both theories, the framework for the material model has been established for future developments.

The developed calibration strategy and the mechanical representation of the forming and springback process techniques have exhibited sufficient flexibility for integration with the PFEPE assisted material model. However, the predicted results (Fig. 16) deviate significantly from the experimental observations, showing the correct trend but a notable gap of approximately 40%. The authors believe that this gap may be related to the as-yet unexplained initial impact of low charge pulses on springback levels. Further investigations will be required to elucidate this phenomenon.

7. Conclusions

This work investigates the post-forming electro plastic effect (PFEPE) on springback reduction for a 0.8 mm thickness AA5754H22 material. The study includes experimental observations of springback reduction at both room and cryogenic temperatures, an evaluation of the potential skin-effect phenomenon in thin samples, and the development of a material model incorporating PFEPE. Based on the developed research and considering the specific material, sample geometry, and electric pulse train, the following conclusions can be drawn.

- Experimental results demonstrate that the post-forming electroplastic effect (PFEPE) effectively reduces springback by approximately 40%–100%. Based on previous findings from the authors (Liu et al., 2022), it is possible to achieve an effective springback reduction of 80% without compromising material strength by applying pulses of less than 3000 A ms/mm^2.
- Under the studied pulse and geometry conditions, the skin effect induces minimal heterogeneity and does not significantly impact behaviour during bending. It is important to note that these conclusions are specific to the studied thin sample with dimensions of 0.8 mm in thickness and a 2.5 mm^2 cross-sectional area; different conclusions may arise with thicker samples.
- Direct stress reduction alone cannot explain or predict the sudden springback decrease observed with low charge pulses.

In view of the results of this study, the following open questions remain unresolved.

- The primary phenomenon driving the springback reduction remains unclear. The comparison between room temperature and cryogenic testing suggests that either a small amount of thermal energy is sufficient to relax dislocations or that athermal effects play a significant role in dislocation relaxation. However, given that only three samples were tested under these conditions, further studies are necessary to provide a more robust evaluation of these conclusions.
- It is unclear the physical phenomenon leading to the initial shock impact effect.
- The current study implemented the electrical pulses parallel to the main deformation mode (in the longitudinal direction of the strip). However, it has not been analysed if applying the electrical pulses perpendicular to the main deformation mode (though thickness), which is the main final goal, will lead to the same reduction.
- As previously noted, the conclusions drawn from this study are specific to the tested material, sample geometry, and pulse characteristics. The findings needs to be expanded and tested in other materials and conditions.

CRediT authorship contribution statement

Jokin Lozares: Methodology. **Nagore Otegi:** Writing – review & editing. **Javier Trinidad:** Writing – review & editing. **Manex Barrenetxea:** Software. **Iosu Aizpuru:** Resources. **Pello Jimbert:** Validation, Methodology. **Joseba Mendiguren:** Writing – original draft, Project administration, Funding acquisition, Formal analysis, Conceptualization.

Declaration of generative AI and AI-assisted technologies in the writing process

During the preparation of this work the author(s) used ChatGPT-3.5in order to improve the English. After using this tool/service, the author(s) reviewed and edited the content as needed and take(s) full responsibility for the content of the publication.

Declaration of competing interest

The authors declare the following financial interests/personal relationships which may be considered as potential competing interests: Joseba Mendiguren reports financial support was provided by Spain Ministry of Science and Innovation. If there are other authors, they declare that they have no known competing financial interests or personal relationships that could have appeared to influence the work reported in this paper.

Data availability

Data will be made available on request.

Acknowledgements

The authors would like to acknowledge the hard work developed by Xabier López De Murillas and Ana Orallo that led to the capabilities to run the experiments in this work. In addition, they would like to acknowledge the financial support of the Basque Government POST-ELEC funded on the Proyectos de investigación program (PI_2017_1_0047) to build the electric pulse generator. Last but not least, the authors would like to acknowledge the financial support of Ministerio de Ciencia e Innovación « Proyectos de Generación de Conocimiento » PID 2022-139130OA-I00, for the ongoing development.

References

A, alco Metals Ltd, EN AW 5754 H22 Sheet and Plate Datasheet, 2023 file:///C:/Users/jmendiguren/Downloads/Aalco-Metals-Ltd_Aluminium-Alloy-5754-H22-Sheet-and-Plate_153.pdf.

Agirre, J., Galdos, L., Saenz de Argandoña, E., Mendiguren, J., 2018. Hardening prediction of diverse materials using the Digital Image Correlation technique. Mech. Mater. 124, 71–79. https://doi.org/10.1016/j.mechmat.2018.05.007.

D. Banabic, O. Cazacu, T. Kuwabara, Anisotropy and Formability, (n.d.).

Bao, J., Chen, W., Bai, J., Xu, J., Shan, D., Guo, B., 2022. Local softening deformation and phase transformation induced by electric current in electrically-assisted micro-compression of Ti–6Al–4V alloy. Mater. Sci. Eng. 831, 142262 https://doi.org/10.1016/j.msea.2021.142262.

Burch, I., Gilchrist, J., 2018. Survey of global activity to phase out internal combustion engine vehicles. https://theclimatecenter.org/wp-content/uploads/2018/09/Survey-on-Global-Activities-to-Phase-Out-ICE-Vehicles-FINAL.pdf.

Caloz, G., Dauge, M., Faou, E., Péron, V., 2011. On the influence of the geometry on skin effect in electromagnetism. Comput. Methods Appl. Mech. Eng. 200, 1053–1068. https://doi.org/10.1016/j.cma.2010.11.011.

Chaabani, S., Rodriguez, I., Cuesta, M., Ayed, Y., Arrazola, P.J., Germain, G., 2019. Tool wear and cutting forces when machining inconel 718 under cryogenic conditions: liquid nitrogen and carbon dioxide. https://doi.org/10.1063/1.5112610.

Choi, Y., Lee, J., Panicker, S.S., Jin, H.-K., Panda, S.K., Lee, M.-G., 2020. Mechanical properties, springback, and formability of W-temper and peak aged 7075 aluminum alloy sheets: experiments and modeling. Int. J. Mech. Sci. 170, 105344 https://doi.org/10.1016/j.ijmecsci.2019.105344.

de Souza, E.A., Peric, D., Owen, D.R.J., 2008. Computational Methods for Plasticity. Wiley.

Edwards, T.C., Steer, M.B., 2016. Foundations for Microstrip Circuit Design. John Wiley \& Sons.

Egeskog, A., Hagdahl, K.-H., Krewer, C., Råde, I., Bolin, L., 2021. Carbon Footprint Report Battery Electric XC40 Recharge and the XC40 ICE.

García, A., Monsalve-Serrano, J., Martinez-Boggio, S., Tripathi, S., 2022. Techno-economic assessment of vehicle electrification in the six largest global automotive markets. Energy Convers. Manag. 270, 116273 https://doi.org/10.1016/j.enconman.2022.116273.

Grimm, T.J., Mears, L.M., 2022. Skin effects in electrically assisted manufacturing. Manufacturing Letters 34, 67–70. https://doi.org/10.1016/j.mfglet.2022.09.006.

Grosso, M., Cristinel Raileanu, I., Krause, J., Alonso Raposo, M., Duboz, A., Garus, A., Mourtzouchou, A., Ciuffo, B., 2021. How will vehicle automation and electrification

affect the automotive maintenance, repair sector? Transp. Res. Interdiscip. Perspect. 12, 100495 https://doi.org/10.1016/j.trip.2021.100495.
Hariharan, K., Lee, M.G., Kim, M.J., Han, H.N., Kim, D., Choi, S., 2015. Decoupling thermal and electrical effect in an electrically assisted uniaxial tensile test using finite element analysis. Metall. Mater. Trans. A 46, 3043–3051. https://doi.org/10.1007/s11661-015-2879-3.
Hetz, P., Suttner, S., Merklein, M., 2020. Investigation of the springback behaviour of high-strength aluminium alloys based on cross profile deep drawing tests. Procedia Manuf. 47, 1223–1229. https://doi.org/10.1016/j.promfg.2020.04.187.
Hou, H., Zhao, G., Yu, J., Sun, Y., Li, H., 2023. Experimental studies and modeling of strain rate- and temperature-dependent springback behavior of hot-deformed aluminum alloys. J. Mater. Process. Technol. 318, 118029 https://doi.org/10.1016/j.jmatprotec.2023.118029.
Humphreys, F.J., Hatherly, M., 2004. Recovery after Deformation, Recrystallization and Related Annealing Phenomena, pp. 169–213. https://doi.org/10.1016/B978-008044164-1/50010-4.
Kang, W., Beniam, I., Qidwai, S.M., 2016. In situ electron microscopy studies of electromechanical behavior in metals at the nanoscale using a novel microdevice-based system. Rev. Sci. Instrum. 87 https://doi.org/10.1063/1.4961663.
Kim, S.-J., Kim, S.-D., Yoo, D., Lee, J., Rhyim, Y., Kim, D., 2016. Evaluation of the athermal effect of electric pulsing on the recovery behavior of magnesium alloy. Metall. Mater. Trans. 47, 6368–6373. https://doi.org/10.1007/s11661-016-3804-0.
Leo, P., D'Ostuni, S., Casalino, G., 2016. Hybrid welding of AA5754 annealed alloy: role of post weld heat treatment on microstructure and mechanical properties. Mater. Des. 90, 777–786. https://doi.org/10.1016/j.matdes.2015.10.150.
Li, X., Zhu, Q., Hong, Y., Zheng, H., Wang, J., Wang, J., Zhang, Z., 2022. Revealing the pulse-induced electroplasticity by decoupling electron wind force. Nat. Commun. 13, 6503. https://doi.org/10.1038/s41467-022-34333-2.
Li, H., Jin, F., Zhang, M., Ding, J., Bian, T., Li, J., Ma, J., Zhang, L., Wang, Y., 2023. Decoupling electroplasticity by temporal coordination design of pulse current loading and straining. Materials Science and Engineering: A 881, 145435. https://doi.org/10.1016/j.msea.2023.145435.
Liu, Y., Wang, L., Zhu, B., Wang, Y., Zhang, Y., 2018. Identification of two aluminum alloys and springback behaviors in cold bending. Procedia Manuf. 15, 701–708. https://doi.org/10.1016/j.promfg.2018.07.303.
Liu, S., Zhu, J., Lin, X., Wang, X., Wang, G., 2021. Coupling effect of stretch-bending deformation and electric pulse treatment on phase transformation behavior and superelasticity of a Ti-50.8 at.% Ni alloy. Mater. Sci. Eng. 799, 140164 https://doi.org/10.1016/j.msea.2020.140164.
Liu, W., Otegi, N., Orallo, A., Barrenetxea, M., Aizpuru, I., Lian, J., Mendiguren, J., 2022. Post-forming, electro-plastic effect internal stress reduction in AA5754 aluminium alloy. Mater. Sci. Eng. 852, 143686 https://doi.org/10.1016/j.msea.2022.143686.
Liu, J., Jia, D., Fu, Y., Kong, X., Lv, Z., Zeng, E., Gao, Q., 2024. Electroplasticity effects: from mechanism to application. Int. J. Adv. Des. Manuf. Technol. 131, 3267–3286. https://doi.org/10.1007/s00170-023-12072-y.
Marciniak, Z., Duncan, J., 2002. Mechanics of Sheet Metal Forming. Elsevier. https://doi.org/10.1016/B978-0-7506-5300-8.X5000-6.
Mendiguren, J., Trujillo, J.J., Cortés, F., Galdos, L., 2013. An extended elastic law to represent non-linear elastic behaviour: application in computational metal forming. Int. J. Mech. Sci. 77, 57–64. https://doi.org/10.1016/j.ijmecsci.2013.09.026.
Mendiguren, J., Galdos, L., de Argandoña, E.S., 2018. On the plastic flow rule formulation in anisotropic yielding aluminium alloys. Int. J. Adv. Manuf. Technol. 99, 255–274. https://doi.org/10.1007/s00170-018-2512-x.
Modaresi, R., Müller, D.B., 2012. The role of automobiles for the future of aluminum recycling. Environ. Sci. Technol. 46, 8587–8594. https://doi.org/10.1021/es300648w.
Morte, I.B.B., Araújo, O. de Q.F., Morgado, C.R.V., de Medeiros, J.L., 2023. Electrification and decarbonization: a critical review of interconnected sectors, policies, and sustainable development goals. Energy Storage and Saving. https://doi.org/10.1016/j.enss.2023.08.004.
Oyamada, K., Peschansky, V.G., Stepanenko, D.I., 1990. Static skin effect at high current densities. Phys. B Condens. Matter 165–166, 277–278. https://doi.org/10.1016/S0921-4526(90)80988-U.
Pitchure, D.J., Ricker, R.E., 2007. The Recovery of Elastic Properties at 35 ° C in TRIP 700 Steel Following Deformation, vol. 16, pp. 349–353. https://doi.org/10.1007/s11665-007-9061-z.
Raicevic, N.B., Aleksic, S.R., Iatcheva, I., Barukcic, M., 2020. Enhanced method for pulse skin effect calculation of cylindrical conductors. COMPEL 39, 623–635. https://doi.org/10.1108/COMPEL-10-2019-0382.
Rivas, R.A., Marti, J.R., 2002. Calculation of frequency-dependent parameters of power cables: matrix partitioning techniques. IEEE Power Eng. Rev. 22 https://doi.org/10.1109/MPER.2002.4312322, 64–64.
Salandro, W.A., Jones, J.J., Bunget, C., Mears, L., Roth, J.T., 2015. Electrically Assisted Forming. Springer International Publishing, Cham. https://doi.org/10.1007/978-3-319-08879-2.
Schmiedt, M., Schneider, R., Hezler, C., Grant, R.J., Rimkus, W., Schlosser, J.M., Jung, J., Harrison, D.K., 2022. Repurposing steel press production lines for hot formed high-strength aluminium automotive body components. Advances in Industrial and Manufacturing Engineering 4, 100080. https://doi.org/10.1016/j.aime.2022.100080.
Schuster, P.A., Österreicher, J.A., Kirov, G., Sommitsch, C., Kessler, O., Mukeli, E., 2019. Characterisation and comparison of process Chains for producing automotive structural parts from 7xxx Aluminium Sheets. Metals 9, 1–15. https://doi.org/10.3390/met9030305.
Seran, E., Godefroy, M., Pili, E., Michielsen, N., Bondiguel, S., 2017. What we can learn from measurements of air electric conductivity in 222 Rn-rich atmosphere. Earth Space Sci. 4, 91–106. https://doi.org/10.1002/2016EA000241.
Shivaprasad, C., Subrahmanyam, A., Reddy, N.V., 2023. Effect of electric path in electric pulse aided V-bending of Ti-6Al4V: an experimental and numerical study. J. Manuf. Process. 100, 75–84. https://doi.org/10.1016/j.jmapro.2023.05.018.
Silvestre, E., Garcia, D., Galdos, L., De Argandoña, E.S., Mendiguren, J., 2016. Roll levelling semi-analytical model for process optimization. In: Journal of Physics: Conference Series. https://doi.org/10.1088/1742-6596/734/3/032034.
Sun, X., Ji, Y., Xiao, A., Wang, S., Cui, X., 2022. Influence of single-pulse and high-amplitude current on springback and mechanical properties of AA5052 aluminum alloy sheets. Mater. Char. 194, 112337 https://doi.org/10.1016/j.matchar.2022.112337.
T.E. parliament and the Council, 2021. COM (2021) 556: Proposal for a REGULATION of the EUROPEAN PARLIAMENT and of the COUNCIL Amending Regulation (EU) 2019/631 as Regards Strengthening the CO2 Emission Performance Standards for New Passenger Cars and New Light Commercial Vehicles in Line with.
The Engineering ToolBox (2016), 2023. Permeability. https://www.engineeringtoolbox.com/permeability-d_1923.html.
Tiwari, J., Pratheesh, P., Bembalge, O.B., Krishnaswamy, H., Amirthalingam, M., Panigrahi, S.K., 2021. Microstructure dependent electroplastic effect in AA 6063 alloy and its nanocomposites. J. Mater. Res. Technol. 12, 2185–2204. https://doi.org/10.1016/j.jmrt.2021.03.112.
Viereck, D., Lohe, D., Vohringer, O., Macherauch, E., Werkstoffwissenschaften, F., 1991. Relaxation of residual stresses in a nickel-base superalloy due to dislocation creep. Strength of Metals and Alloys 1, 367–372.
Wolfram, P., Tu, Q., Heeren, N., Pauliuk, S., Hertwich, E.G., 2021. Material efficiency and climate change mitigation of passenger vehicles. J. Ind. Ecol. 25, 494–510. https://doi.org/10.1111/jiec.13067.
Xiao, H., Jiang, S., Zhang, K., Jia, Y., Shi, C., Lu, Z., Jiang, J., 2020. Optimizing the microstructure and mechanical properties of a cold-rolled Al–Mg–Li alloy via electropulsing assisted recrystallization annealing and ageing. J. Alloys Compd. 814, 152257 https://doi.org/10.1016/j.jallcom.2019.152257.
Xu, Z., Jiang, T., Huang, J., Peng, L., Lai, X., Fu, M.W., 2022. Electroplasticity in electrically-assisted forming: process phenomena, performances and modelling. Int. J. Mach. Tool Manufact. 175, 103871 https://doi.org/10.1016/j.ijmachtools.2022.103871.
Yan, S., Chen, X., 2023. Time-domain analytical solutions to pulsed eddy current model of moving cylindrical conductor. NDT E Int. 137, 102863 https://doi.org/10.1016/j.ndteint.2023.102863.
Yuan, X., Lei, B., Li, Z., Qi, W., 2015. Skin effect analysis for pulse current in the PEA based on frequency domain method. IEEE Trans. Plasma Sci. 43, 1611–1616. https://doi.org/10.1109/TPS.2015.2417055.
Zaefferer, S., 2021. Interacting with current. Nat. Mater. 20, 448–449. https://doi.org/10.1038/s41563-021-00964-x.
Zhang, X., Li, H., Zhan, M., Shao, G., Ma, P., 2018. Extraordinary effect of the δ phase on the electrically-assisted deformation responses of a Ni-based superalloy. Mater. Char. https://doi.org/10.1016/j.matchar.2018.08.018.
Zhao, W., Liu, D., Zhang, X., Zhang, H., Liu, J., Ma, C., Zhang, R., Dong, Y., Ye, C., 2020. The effect of electropulsing-assisted ultrasonic nanocrystal surface modification on the microstructure and properties of 300M steel. Surf. Coating. Technol. 397, 125994 https://doi.org/10.1016/j.surfcoat.2020.125994.